RSC Advances

PAPER

View Article Online
View Journal | View Issue

CrossMark click for updates

Cite this: *RSC Adv.*, 2016, **6**, 95369

Photocatalytic WO_3/TiO_2 nanowires: WO_3 polymorphs influencing the atomic layer deposition of TiO_2†

Dávidné Nagy,*[ab] Tamás Firkala,[b] Eszter Drotár,[c] Ágnes Szegedi,[c] Krisztina László[d] and Imre Miklós Szilágyi[be]

50–70 nm hexagonal (h-) and 70–90 nm monoclinic (m-) WO_3 nanoparticles (NPs) were prepared by controlled annealing of $(NH_4)_xWO_3$ in air at 470 and 600 °C, respectively. In addition, 5–10 nm thick and several micrometer long h-WO_3 nanowires (NWs) were obtained by microwave hydrothermal synthesis at 160 °C with Na_2WO_4, HCl and $(NH_4)_2SO_4$ as starting materials. TiO_2 was deposited on h-WO_3 NWs by atomic layer deposition (ALD) at 300 °C using $Ti(^iOPr)_4$ and H_2O as precursors. The as-prepared materials were studied by TG/DTA-MS, XRD, Raman, SEM-EDX, TEM, ellipsometry, UV-Vis, and their photocatalytic activity was also tested by the photodecomposition of aqueous methyl orange. Our study is the first evidence of diverse ALD nucleation on various WO_3 polymorphs, since on h-WO_3 NWs TiO_2 nucleated only as particles, whereas on m-WO_3 conformal TiO_2 film was formed, explained by the different surface OH coverage of h- and m-WO_3. The h-WO_3 NWs had significantly higher photocatalytic activity compared to h-WO_3 NPs, and similar performance as m-WO_3 NPs. By adding TiO_2 to h-WO_3 NWs by ALD method, the photocatalytic performance increased by 65%, showing clearly the uniqueness of ALD to obtain superior oxide composite photocatalysts.

Received 25th July 2016
Accepted 30th September 2016

DOI: 10.1039/c6ra18899k

www.rsc.org/advances

Open Access Article. Published on 30 September 2016. Downloaded on 1/22/2026 5:10:50 PM.
This article is licensed under a Creative Commons Attribution 3.0 Unported Licence.

Introduction

Water scarcity and the purity of available water resources around the world are concerning issues of our century.[1,2] Semiconductor photocatalysis received substantial attention recently to address environmental remediation challenges such as purifying water sources.[3–7] It was presented that using solar energy the purification of water is possible from toxic compounds such as certain pharmaceutical drugs, bacteria or herbicids *etc.*[8,9] Among semiconductor oxides TiO_2 is one of the most studied photocatalyst since its valence and conductance energy levels are suitable for both oxidation and reduction of water molecules (water splitting).[10–17] However, the utilization of TiO_2 is hugely limited by its restricted light absorption properties to the UV range. Therefore, besides TiO_2, the photocatalytic activity of several other semiconductor oxides was also studied (*e.g.* V_2O_5, WO_3, ZnO, ZrO_2).[18–24] Nanostructured WO_3 can absorb part of the Visible spectrum, making it the second most studied oxide for visible-responsive photocatalysis.[25]

Another limiting factor of TiO_2 is the relatively fast recombination of the photo-induced charges. One approach to improve the photocatalytic performance of a semiconductor oxide is forming composite photocatalysts with other semiconductors. An important benefit of forming composite nanostructures could be the reduced recombination rate of the photo-generated charges by effective charge transfer between the two semiconductor oxide. In the case of type II band alignment where one of the nanostructure has both the valence and conduction band energies lower positioned than the respective bands of the counterpart effective separation of the charge carriers can take place.[26] In addition to the production of longer-lived charges, the heterostructure can benefit from Vis activity if a UV active photocatalyst such as TiO_2 is coupled with semiconductor oxides absorbing in the visible region. TiO_2/WO_3 is such a system and several studies showed that such nanocomposite heterostructures have superior photocatalytic activities over single semiconductors.[27–30]

It is also known that the photocatalytic activity is a complex function of several factors such as the crystal structure, morphology or optical properties of the material *etc.*[31,32] In order to achieve high performance photocatalysts maximizing the surface area of the material is a general approach. Therefore,

[a]*Institute for Materials and Processes, School of Engineering, The University of Edinburgh, The King's Buildings, Mayfield Road, Edinburgh, EH9 3JL, UK. E-mail: davidne.nagy@gmail.com*

[b]*Department of Inorganic and Analytical Chemistry, Budapest University of Technology and Economics, Szent Gellért tér 4., Budapest, H-1111, Hungary*

[c]*Hungarian Academy of Sciences, Institute of Materials and Environmental Chemistry, Magyar tudósok körútja 2., Budapest, H-1117, Hungary*

[d]*Department of Physical Chemistry and Materials Science, Budapest University of Technology and Economics, Budafoki út 8., Budapest, H-1111, Hungary*

[e]*MTA-BME Technical Analytical Research Group of the Hungarian Academy of Sciences, Szent Gellért tér 4., Budapest, H-1111, Hungary*

† Electronic supplementary information (ESI) available. See DOI: 10.1039/c6ra18899k

Open Access Article. Published on 30 September 2016. Downloaded on 1/22/2026 5:10:50 PM.
This article is licensed under a Creative Commons Attribution 3.0 Unported Licence.

several techniques have been adopted to fabricate nanostructured oxide photocatalysts. Among the reported nanostructures, nanofibers have received immense attention due to their high surface-to-volume ratio, good optical, electric and chemical properties.[33,34]

Previous studies revealed that WO_3/TiO_2 1D photocatalysts have huge potential.[35–38] Unfortunately, WO_3 is quite difficult to prepare with very small dimensions. The smallest forms of the most studied WO_3 polymorph, *i.e.* monoclinic (m-) WO_3 have been 10–100 nm as particles, or 50–200 nm as nanofibers.[39–41] Nevertheless, m-WO_3 is a widespread photocatalyst. In contrast, the second most important WO_3 modification, *i.e.* hexagonal (h-) WO_3, has been studied in photocatalysis only once, and its photocatalytic activity was lower compared to m-WO_3.[42] It was explained by that unlike the completely oxidized m-WO_3, h-WO_3 always contain some cation (*e.g.* Na^+, K^+, NH_4^+) impurities in its hexagonal channels, which are vital for stabilizing the metastable structure.[43,44] Besides, h-WO_3 contains also partially reduced W atoms, which may serve as recombination centers during the photocatalytic reaction, decreasing the activity.[43] However, h-WO_3 has been prepared recently in the form of very fine nanowires with *ca.* 5–10 nm thickness, which is a very promising morphology for photocatalysis, but unfortunately their photocatalytic properties have not been tested yet.

Recently it was reported that m-WO_3/TiO_2 core/shell nanofibers, where the shell layer was deposited by atomic layer deposition (ALD), had excellent photocatalytic properties due to the synergy of WO_3 and TiO_2.[45] ALD is based on successive, alternating surface controlled reactions from the gas phase to produce highly conformal and uniform thin films with thickness control of sub-nanometer precision. Thus, ALD provides new strategies in modifying the properties of nanoscaled materials and new synthetic routes to novel nanostructures.[46–52]

In the above example the m-WO_3 nanofibers were 200–300 nm thick. Thus, it is logical to expect better photocatalytic properties, if WO_3 1D nanostructures with even smaller dimensions can be used as substrates. The now available 5–10 nm thick h-WO_3 fibers are good candidates for employing in WO_3/TiO_2 photocatalysts with improved properties.

In this study, we obtained h-WO_3 NWs by microwave assisted hydrothermal synthesis at 160 °C with Na_2WO_4, HCl and Na_2SO_4 as starting materials. ALD was the method of choice to put TiO_2 onto the h-WO_3 nanowires, since it has the capability to deposit very thin layers on highly structured surfaces. The TiO_2 layer was deposited at 300 °C using $Ti(^iOPr)_4$ and H_2O as precursors, and it was designed to have around 3 nm thickness because previous studies showed that thin TiO_2 nanolayers could significantly enhance the photo-efficiency of the nanosized WO_3.[45] It must be noted that up to now ALD growth has been done only on m-WO_3, but not on h-WO_3. Since the two polymorphs have different surface properties,[42] this allowed us to study the characteristics of ALD nucleation on the surface of various WO_3 crystalline structures, which was not yet reported in the literature to the best of our knowledge.

For comparison, we also prepared hexagonal (h-) and monoclinic (m-) WO_3 nanoparticles (NPs) by controlled annealing of $(NH_4)_xWO_3$ in air at 470 and 600 °C, respectively. In addition, we prepared an m-WO_3/TiO_2 composite by annealing the h-WO_3/TiO_2 sample at 600 °C in air. It is well established that at this temperature the h-WO_3 structure transforms into m-WO_3. Usually when m-WO_3 is formed thermally from nanostructured precursors, it will be present in the form of 50–200 nm particles.[53] However, we aimed to test whether the TiO_2 coating might prevent the morphology change, and m-WO_3/TiO_2 with nanowire morphology could be obtained.

The obtained materials were studied by TG/DTA-MS, XRD, Raman, SEM-EDX, TEM, ellipsometry, UV-Vis, and their photocatalytic activity was tested by UV-Vis through the photobleaching of aqueous methyl orange.

Experimental

Preparation methods

Hexagonal (h-) and monoclinic (m-) WO_3 nanoparticles (NPs) were prepared by annealing hexagonal ammonium tungsten bronze, $(NH_4)_xWO_{3-y}$ in air at 470 °C and 600 °C, respectively.[34,54]

For the preparation of h-WO_3 nanowires (NWs) a microwave-assisted hydrothermal synthesis method was applied.[44] 1.5 g $Na_2WO_4 \cdot 2H_2O$ was dissolved in 33.75 ml H_2O, then under stirring 3.75 ml 3 M HCl was added dropwise, and finally 22.5 ml 0.5 M $(NH_4)_2SO_4$ was introduced. The as-prepared solution was heated to 160 °C in 20 min, and then kept at 160 °C for 3 hours in a Synthos 3000 Anton Paar microwave reactor. The solid reaction product was centrifuged, washed two times with water, once with ethanol, and again two times with water. In each washing step, 45 ml solvent was poured over the crystals; the dispersion was stirred for 1 min, and centrifuged for 5 min at 6000 min^{-1}. Finally, the as-prepared h-WO_3 NWs were dried at 80 °C for 12 hours. The yield was 64%.

The h-WO_3/TiO_2 nanowire composite was prepared by depositing a TiO_2 nanolayer onto the surface of the as-prepared h-WO_3 NWs by atomic layer deposition (ALD). The ALD reaction was carried out at 300 °C in a Picosun SUNALE R-100 type reactor. 100 ALD cycles were applied using $Ti(O^iPr)_4$ (60 °C evaporation temperature) and H_2O as precursors, with 1 s pulse and 30 s purge times for both precursors.

The m-WO_3/TiO_2 composite sample was obtained by annealing the h-WO_3/TiO_2 sample at 600 °C in air.

Characterization methods

Thermal analysis was used to investigate the influence of washing steps during the h-WO_3 NW preparation and to check the thermal stability of as-synthesized h-WO_3 NWs. For this an STD 2960 simultaneous TG/DTA device (TA Instruments Inc.) was used, which was on-line coupled to a Thermostar GSD 200 quadruple mass spectrometer (Balzers Instruments) through a heated (200 °C), 100% silanated quartz capillary (D = 0.15 mm). During the TG/DTA-MS measurements, samples (*ca.* 100 mg) were heated in a Pt crucible at 10 °C min^{-1} heating rate in flowing air (130 ml min^{-1}). The fragments of the evolved gases were monitored by Multiple Ion Detection (MID) mode in the 1–64 m/z range.

 This journal is © The Royal Society of Chemistry 2016

Open Access Article. Published on 30 September 2016. Downloaded on 1/22/2026 5:10:50 PM. This article is licensed under a Creative Commons Attribution 3.0 Unported Licence.

The crystal phases were determined by recording the XRD pattern of the samples by a PANalytical X'pert Pro MPD X-ray diffractometer using Cu Kα radiation.

The Raman spectra provided further information on the crystal structure and the bonds. A Jobin–Yvon Labram type spectrophotometer equipped with an Olympus BX-41 microscope was used. For excitation source a frequency-doubled Nd–YAG laser (532 nm) was employed. The scattered photons were collected by a CCD type detector.

To investigate the optical properties of the catalysts, UV-Vis diffuse reflectance spectra were recorded by a Cary 100 UV-Vis spectrophotometer equipped with a DRA-CA-30I type integration sphere.

For the study of the morphology and composition, SEM-EDX and TEM measurements were applied. A LEO 1540XB type RÖNTEC FEG SEM microscope equipped with a Quantax EDX detector was used for the SEM-EDX recordings. The TEM images were provided by a FEI Morgagni 268D type TEM microscope employing a tungsten cathode.

For determining the apparent surface area of the photocatalysts, the BET model was used. The low temperature nitrogen adsorption measurement was conducted in a NOVA 2000E type (Quantachrome, USA) device at the temperature of liquid nitrogen.

For estimating the ALD TiO_2 film thickness, a TiO_2 film was deposited on a Si wafer by ALD, using 300 cycles and the same precursors, pulse and purge times, as in the case of h-WO_3 NW substrates. The film thickness was determined by ellipsometry. The spectra were recorded by a Woollam M-2000DI ellipsometer between 400 and 1500 nm.

Photocatalysis

The photocatalytic efficiencies of the as-prepared catalysts were tested in the photo-bleaching reaction of methyl-orange (MO). The concentration of the catalyst and the methyl orange were 100 mg/350 ml and 10 mg/350 ml, respectively. A Heraus TQ 150 mercury immersion lamp (radiation flux, Φ: 200–600 nm 47 W, strongest spectral lines: 254 nm: 4 W, 313 nm: 4.3 W, 366 nm: 6.4 W, 405 nm: 3.2 W, 436 nm: 4.2 W, 546 nm: 5.1 W, 577 nm: 4.7 W) was applied in a Heraus type cylindrical glass photo-reactor. The experiments were conducted under oxygen bubbling at room temperature assured by the continuous water circulation through the cooling jacket of the lamp. At first the solution was kept in dark for 15 min, to reach the adsorption equilibrium between the catalyst and the dye. Then the lamp was switched on and 3 ml samples were taken in every 30 min using a syringe equipped with filter (Sigma Aldrich, Iso-Disc, PTFE, 0.45 μm pore size membrane). The decline of the MO concentration was followed by a Jasco V-550 type UV-Vis spectrophotometer at 465 nm.

Results and discussion

Formation mechanism of h-WO_3 nanowires

The fabrication of nano-sized WO_3 by wet-chemical synthesis approaches such as hydrothermal (HT) synthesis is a popularly applied method for cheap and versatile nanostructure formulation.[44,55] To direct crystal growth in HT synthesis various structure directing agents were presented in the literature from simple inorganic salts like Na_2SO_4, NH_4NO_3 to complex organic structures like oxalic acid or poly-ethylene glycol.[33,55,56] To fabricate delicate h-WO_3 nanowires in this paper $(NH_4)_2SO_4$ was used following an earlier report.[44] It is believed that the capping agents such as $(NH_4)_2SO_4$ dictate anisotropic 1D growth by selectively binding to specific crystal facets of the initial crystal nuclei of WO_3. The adsorption of capping agents increases the surface energy of the selected facets leading to inhibited crystal growth rates and resulting in the formation of 1D nanostructures.[44] It is also known that several other factors may contribute to the morphology and crystal phases of the final nanomaterials such as time, temperature or the pH.[31,55,57] This latter one plays an especially important role in the formation of WO_3 since H^+ is essential to form tungstic acid from the selected tungsten precursor which is typically a tungstate. Then WO_3 is formed according to eqn (1).

$$WO_4^{2-} + 2H^+ \leftrightarrow H_2WO_4 \xleftrightarrow{T\ (^\circ C)} WO_3 + H_2O \qquad (1)$$

Thermal analysis

The role of washing steps in reaching pure h-WO_3 nanowires after the microwave hydrothermal reactions was studied by TG/DTA-MS measurement. The results (presented in detail in the ESI†) confirmed that washing steps were effective and removed all precursors and reactants. The as-prepared, non-washed, only dried h-WO_3 NW samples contained significant amount from not used reagents, *i.e.* $(NH_4)_2SO_4$, HCl, and water as well, from which various gaseous products were detected in air, *e.g.* H_2O, NH_3, from the decomposition of NH_4^+, NO and N_2O from the combustion of NH_3, HCl, SO and SO_2 from the decomposition of SO_4^{2-} (ref. 58) (Table S1†). When the sample was annealed, until 100 °C small amount of adsorbed H_2O was released in an endothermic reaction (Fig. S1 and S2†). Then between 150–300 °C H_2O and NH_3 evolved accompanied by an endothermic heat effect, whereas between 300–450 °C H_2O, NH_3, NO_x and SO_x gases were detected. The combustion of NH_3 was an endothermic reaction, which changed the DTA curve to endothermic.[59] HCl was released above 450 °C, accompanied by further release of SO_2.

After the washing steps (Fig. S3 and S4†), all impurities were removed, and accordingly the total mass loss until 900 °C decreased from 18.2% to 5.8%. Now only the release of water was observed in two endothermic reactions between 25–200 and 200–450 °C. The metastable hexagonal WO_3 framework was transformed into the thermodynamically stable m-WO_3 at 503 °C in an exothermic reaction. The results confirmed the importance of proper washing steps after the microwave hydrothermal reaction in order to obtain pure h-WO_3 nanowires. The thermal analysis also showed that the cleaned, pure h-WO_3 was stable until 500 °C, therefore performing the ALD reaction at 300 °C was safe.

After the ALD reaction performed at 300 °C-on and 10^3 Pa vacuum the h-WO_3 NWs lost considerable amount of adsorbed

Open Access Article. Published on 30 September 2016. Downloaded on 1/22/2026 5:10:50 PM.
This article is licensed under a Creative Commons Attribution 3.0 Unported Licence.

and structural water (only 2.5% mass loss) (Fig. S6 and S7†). The exothermic DTA peak belonging to the hexagonal–monoclinic WO_3 transformation was at 506 °C.

XRD

The XRD patterns (Fig. 1) served information about the crystalline structure of the samples. No crystalline impurities were detected in any of the samples. All reflection peaks of h-WO_3 NPs were assigned to pure h-WO_3 (ICDD 33-1387). The h-WO_3 NWs exhibited well-defined and intense diffraction peaks supposing high crystallinity of the sample. The crystalline phase was confirmed to be pure h-WO_3. The XRD pattern of m-WO_3 NPs was interpreted as pure monoclinic WO_3 (ICDD 43-1035).

In the diffraction pattern of h-WO_3/TiO_2 nanocomposite (Fig. 1) only the h-WO_3 phase could be identified (ICDD 33-1387). The characteristic reflections of TiO_2 could not be detected in the XRD pattern due to the very thin TiO_2 layer (aimed to be less than 3 nm).

Raman

The crystalline phases of the as-prepared WO_3 nanostructures were confirmed by their Raman spectra as well (Fig. 2), in agreement with the XRD results. The h-WO_3 NPs showed well-defined bands characteristic of h-WO_3. The most intense peak at 785 cm^{-1} along with the bands at 650 and 691 cm^{-1} can be associated with the stretching vibration modes of (O–W–O).[60,61] The bands at 263 and 320 cm^{-1} can be assigned to bending vibrations of W–O–W, whereas at 186 cm^{-1} the lattice vibration mode can be found.[60,62]

The Raman spectrum of h-WO_3 NWs was substantially different from that of the h-WO_3 NPs. One of the deviances was that the h-WO_3 NW exhibited overlapping bands in the region of 600 and 850 cm^{-1}. Another considerable difference was that exclusively in the Raman spectra of h-WO_3 NWs terminal W=O stretching modes were recognizable in the interval of 925–965 cm^{-1}.[60,63–65] These peaks are common for all types of WO_3 hydrates, and in some cases the appearance of these

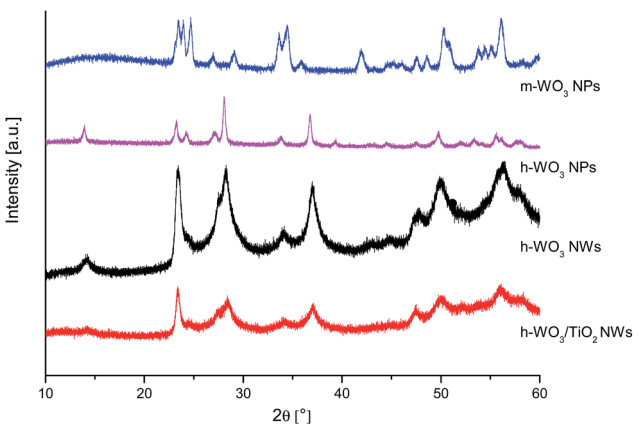

Fig. 1 Powder diffraction pattern of the m-WO_3 NPs, h-WO_3 NPs, m-WO_3 NWs, and h-WO_3/TiO_2 NWs samples.

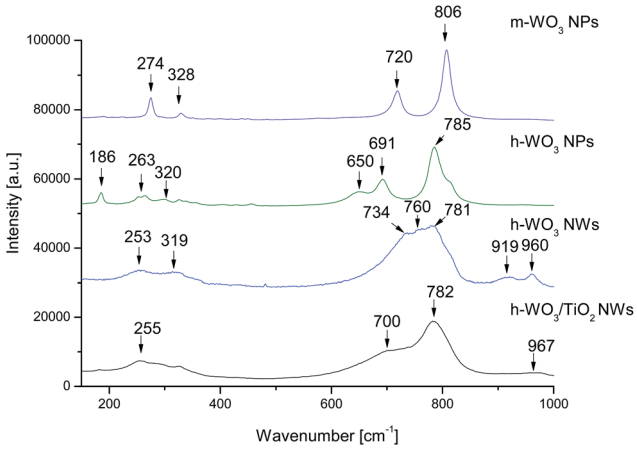

Fig. 2 Raman spectra of the m-WO_3 NPs, h-WO_3 NPs, m-WO_3 NWs, and h-WO_3/TiO_2 NWs samples.

bands were attributed to surface humidity.[43] The absence of these bands in the spectra of h- and m-WO_3 NPs can be ascribed to the high temperature treatment at 500 and 650 °C, respectively. Santato *et al.* reported that the W=O stretching modes in the latter wavenumber interval gradually disappeared by applying increasing annealing temperature in the synthesis process.[63]

The Raman bands of m-WO_3 NPs were in good correspondence with literature values.[66] The peaks were sharp and well-developed supposing good crystallinity of the sample. The bands positioned at 806 and 720 cm^{-1} can be assigned to stretching (O–W–O) vibrational modes. The bands at lower wavelength values belong to (O–W–O) deformation modes.[60]

The Raman bands of h-WO_3/TiO_2 nanocomposite (Fig. 2) were broadened, compared to h-WO_3 NWs. Probably during the ALD deposition some partially reduced W atoms were produced, either due to the conditions (300 °C, 10^3 Pa vacuum) or to the reaction between the precursors and the substrate, and therefore the structure became less ordered. The Raman spectrum is sensitive to the different oxidation states of the atoms due to the change of the chemical bond strength, which resulted in a small shift of the peak positions involving W atoms of different oxidations states.[42] In the h-WO_3/TiO_2 sample the bands involving completely oxidized (+6) and partially reduced (+5, +4) W atoms overlapped, making the peaks broader. The presence of partially reduced tungsten atoms was also indicated by the color change of the sample (it became blue) and by its optical behavior, discussed later. In addition, the terminal W=O stretching modes (above 900 cm^{-1}) of the h-WO_3/TiO_2 nanocomposite had much lower intensities compared to the substrate h-WO_3 NW. The occurred ALD nucleation and the applied temperature and pressure could be accounted for the reduced band intensities.

Characteristic bands of TiO_2 could not be observed as the bands of TiO_2 usually become perceptible above 10 nm film thickness.[45] Similar findings were made by others who found that 1–5% WO_3 loading in a WO_3/TiO_2 nanostructure did not show bands for WO_3 due to low content of WO_3.[67]

This journal is © The Royal Society of Chemistry 2016

Open Access Article. Published on 30 September 2016. Downloaded on 1/22/2026 5:10:50 PM.
This article is licensed under a Creative Commons Attribution 3.0 Unported Licence.

SEM-EDX, TEM

Fig. 3 shows the SEM and TEM images of the prepared catalyst. It was found that the h-WO_3 NPs (Fig. 3a and b) consisted of 50–70 nm nanocrystals. The SEM and TEM images confirmed the formation of uniform and good quality nanowires for the h-WO_3 NWs (Fig. 3c and d) being several micrometer long and *ca.* 5–10 nm thick. On Fig. 3e and f the m-WO_3 NPs can be viewed, consisting of irregularly-shaped nanoparticles with a characteristic dimension of 60–90 nm.

The EDX elemental analysis revealed that h-WO_3 NWs contained 2.82 atom% of Na beside W and O atoms, which can be attributed to stabilizing Na ions in the hexagonal channels.[43]

SEM-EDX results were also obtained about the effectiveness of the washing steps. On the SEM image of the as-prepared, non-washed, dried h-WO_3 NW sample micrometer scale particles of the not used reactants can be also seen, and EDX analysis confirmed the presence of N, Cl and S, besides O, Na and W (Fig. S5†).

In the h-WO_3/TiO_2 NWs the SEM and TEM images (Fig. 4a and b) revealed that the TiO_2 was successfully deposited onto the surface of h-WO_3 NWs in the form of individual nanoparticles. The TiO_2 nanoparticles had the diameter of around 5–10 nm, which corresponds to double thickness obtained by ellipsometry data, and is rationalized by the 3D growth of the TiO_2 particles. This is in agreement with expectations, as in the case of nanoparticle nucleation a 3D ALD growth is taking place. EDX showed 2.64 atom% Ti in the h-WO_3/TiO_2 sample, and confirmed the successful deposition of TiO_2 onto the h-WO_3 NWs.

It was also investigated whether an m-WO_3/TiO_2 composite with nanowire morphology could be obtained by annealing the h-WO_3/TiO_2 sample. According to SEM and TEM images (Fig. 4c and d), the fine nanowire morphology was lost when h-WO_3 transformed into m-WO_3. In the m-WO_3/TiO_2 composite m-WO_3 was present in the form of 30–50 nm particles, some of them being connected to each other in a line, pointing to their h-WO_3 nanowire origin. The TiO_2 could be observed as 10 nm particles on the surface of m-WO_3.

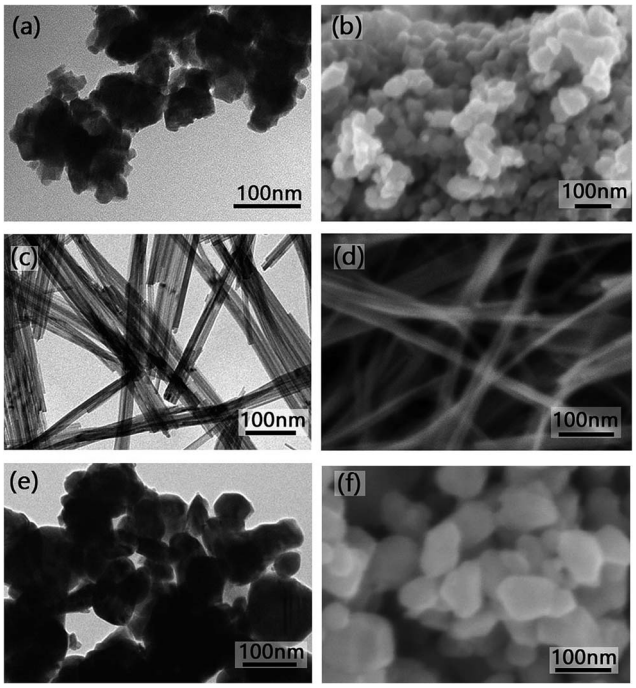

Fig. 3 TEM and SEM images, respectively, of the prepared samples (a, b) h-WO_3 NPs, (c, d) h-WO_3 NWs, (e, f) m-WO_3 NPs.

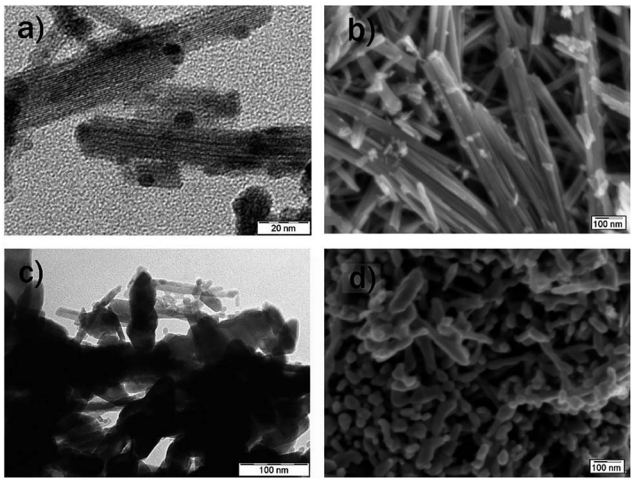

Fig. 4 TEM and SEM images of the (a and b) h-WO_3/TiO_2 NWs catalyst, (c and d) m-WO_3/TiO_2 samples obtained by annealing h-WO_3/TiO_2 NWs.

Apparent surface area

The BET nitrogen adsorption measurements were carried out to compare the surface area of the synthesized WO_3 nanostructures. For h-WO_3 NPs it was found to be 11 m^2 g^{-1}.[68] Whereas the h-WO_3 NWs exhibited a much higher surface area of 101 m^2 g^{-1} which is in good agreement with earlier literature results.[44] The almost an order of magnitude higher surface area of the h-WO_3 NWs relative to the h-WO_3 NPs showed the significant effect of the morphology in the surface area which is considered to be an important factor in photocatalysis. The BET surface area of m-WO_3 nanostructure was found to be the lowest among the WO_3 nanostructures with 6.5 m^2 g^{-1}.[42]

Ellipsometry

The estimation of the equivalent TiO_2 layer thickness was determined by ellipsometry on a reference Si wafer. As the native oxide layer on the Si wafer is approximately 3 nm thick, three times more ALD cycle (300 ALD cycle) were run under the same condition on the reference wafer than during the preparation of the nanocomposite in order to make the estimation more accurate. The approximated equivalent TiO_2 thickness prepared by 100 ALD cycles was calculated as 3.65 nm.

ALD nucleation determined by the surface properties of WO_3 polymorphs

Based on SEM and TEM results, it was found that the TiO_2 nucleation followed a distinct pattern on WO_3 polymorphs. Earlier it was reported that the ALD-deposited TiO_2 formed

Open Access Article. Published on 30 September 2016. Downloaded on 1/22/2026 5:10:50 PM.
This article is licensed under a Creative Commons Attribution 3.0 Unported Licence.

a continuous layer on the surface of electrospun m-WO_3 nanofibers resulting in a core–shell nanocomposite.[45] Our results revealed that for h-WO_3 nanowires, instead of a continuous layer, the deposited TiO_2 formed nanoparticle islands. The surface chemistry of the nanostructures plays a key role in the ALD reaction as the native functional group coverage on the surface serves as first binding sites for the ALD reaction.[69–71] Most probably, the distinct ALD nucleation could be accounted for the different surface OH^- group density of the WO_3 polymorphs. Szilágyi *et al.* reported that based on the XPS spectra the amount of surface OH^- group was 0.52% for the h-WO_3 NPs and 0.70% for m-WO_3 NPs.[42] The nucleation of TiO_2 nanoparticles on the surface of h-WO_3 as opposed to continuous film construction, is probably due to the less available nucleation sites.

UV-Vis absorption

All WO_3 nanostructures regardless of the crystal phase exhibited pale yellow colour, however it was found that h-WO_3/TiO_2 NWs nanocomposite turned into blue after the ALD reaction. Solid phase UV/Vis diffuse reflectance (DR) spectra were recorded and analyzed to reveal the optical behavior of the nanostructures and help to understand the reason for the colour differences. The DR spectra is shown in Fig. 5.

It was observed that the h-WO_3 NWs and NPs exhibited a sharp drop of the absorption around 460 nm and 478 nm respectively. Similarly, m-WO_3 NPs showed an absorption threshold at about 485 nm. These values are typical band edges for nanostructured WO_3.[56,72] It is believed that h-WO_3 nanostructures typically exhibit higher energy band values (therefore appears at lower wavelength) due to structural differences.[73]

For the h-WO_3/TiO_2 nanocomposite it was noted that although TiO_2 has a typical absorption threshold around 390–410 nm,[74] the nanocomposite still exhibited absorption in the whole Vis range. Presumably, the enhanced visible absorption arose from the newly generated in-gap states in the band gap due to the presence of partially reduced W atoms. The reduced W atoms were indicated by Raman spectroscopic results and it is believed to be caused by the high temperature and vacuum used over the course of ALD reaction. The blue appearance of the sample is also an indication of the presence of in-gap states in the far-red region of the visible spectrum.

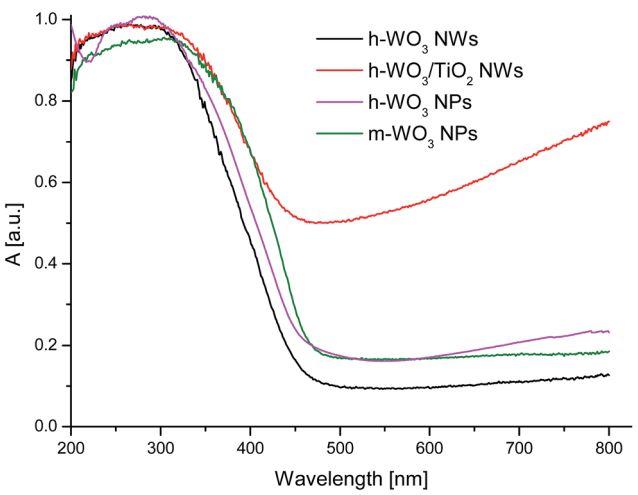

Fig. 5 UV-Vis diffuse reflectance spectra of h-WO_3 NWs, h-WO_3 NPs, m-WO_3 NPs and h-WO_3/TiO_2 NWs samples.

Photocatalysis

The photo-efficiency of the catalysts was modelled in the photo-bleaching reaction of methyl orange under UV-Vis light irradiation (Fig. 6). The relative absorbance was calculated and plotted against time to follow the dye degradation (see on Fig. 6a). Additionally, first-order kinetics could be used to describe the behavior of our data which can be expressed in the following form:

$$\ln\left(\frac{C}{C_0}\right) = kt \quad (2)$$

where C is the dye concentration, C_0 is the initial dye concentration, k is the first-order rate constant and t is time. To test the repeatability of the photocatalytic results multiple experiments were performed. It was found that the experimental error has never exceeded ±4% and was typically 2–3%. The effect of photolysis was negligible under the experimental conditions. The catalysts after the photocatalytic test did not show any visible change *e.g.* in their color.

It was found that the nanowire morphology could enhance significantly the photoactivity of h-WO_3 NWs. Compared to the reference h-WO_3 NPs, the h-WO_3 NWs photo-bleached more than twice as much dye within 4 hours. The enhanced efficiency was reflected on the first-order rate constant values as well, exhibiting 1.72×10^{-3} min^{-1} and 4.93×10^{-4} min^{-1}, respectively. It is generally expected that 1D nanostructures could improve the photocatalytic performance by providing enhanced charge carrier properties and therefore reduced charge recombination.[75] However, in some cases it was revealed that other factors such as the oxidation state of the WO_3 could significantly reduce the photo-bleaching performance despite the 1D morphology.[31] Our results confirmed that there was no such inhibiting factor therefore the nanowire morphology provided an enhanced efficiency over the nanoparticle morphology in the photocatalytic test.

Additionally, the photo-efficiency of the h-WO_3 NWs was comparable to that of the m-WO_3 NPs showing similar rate constant values of 1.72×10^{-3} min^{-1} and 1.79×10^{-3} min^{-1}, respectively. The monoclinic phase WO_3 was reported to exhibit higher photo-efficiency relative to hexagonal WO_3 due to the more oxidized composition,[42] which was confirmed by our results when h-WO_3 and m-WO_3 NPs with similar morphologies were compared. Clearly, beside the prominent effect of the crystal phase, the morphology could play an important role in the determination of the photo-efficiency. The highest photo-degradation was presented by the h-WO_3 NW/TiO_2 nanocomposite. It decomposed 56% of the original dye concentration by the end of the 4 hour reaction, which represents a higher than four times improvement relative to the h-WO_3 NPs and

 This journal is © The Royal Society of Chemistry 2016

Open Access Article. Published on 30 September 2016. Downloaded on 1/22/2026 5:10:50 PM.
This article is licensed under a Creative Commons Attribution 3.0 Unported Licence.

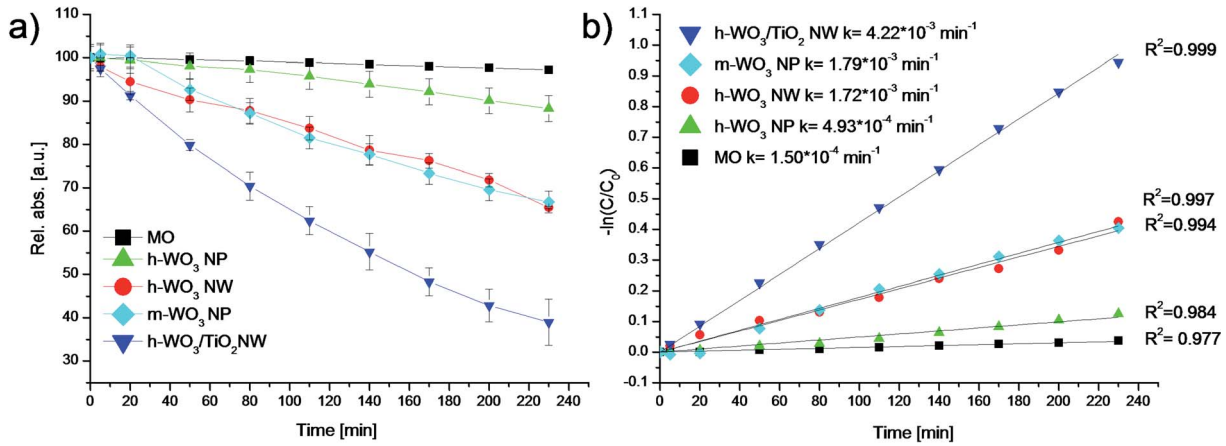

Fig. 6 (a) Photocatalytic degradation curves and (b) linearized first rate kinetic curves of the m-WO_3 NPs, h-WO_3 NPs, h-WO_3 NWs, and h-WO_3/TiO_2 NWs samples.

almost two times better performance relative to the h-WO_3 NWs. Therefore, the highest rate constant of 4.22×10^{-3} min^{-1} was calculated for the h-WO_3 NW/TiO_2 nanocomposite. The enhanced photoactivity can be attributed to the better light utilization due to absorption in the complete UV-Vis spectrum, and reduced recombination of the photo-generated charges through effective charge separation between h-WO_3 and TiO_2. In the literature it was earlier reported that m-WO_3–TiO_2 nanocomposite prepared by depositing TiO_2 onto nanofibers of m-WO_3 by ALD showed improved activities relative to bare WO_3 and TiO_2.[45] However, successful ALD reaction onto h-WO_3 NWs to prepare h-WO_3 NW/TiO_2 nanocomposite has not yet been presented to the best of our knowledge. The advantage of coupling WO_3 with TiO_2 in various crystal phases and morphologies was shown to have a great potential in improving photocatalytic performances.[35,76,77] This was not straightforward, since previously it was observed that in the case of blue h-WO_3 samples with partially reduced W atoms the photocatalytic activity was significantly lower, even compared to yellow h-WO_3 NPs.[42] The reason could be that although the blue h-WO_3 had absorption in the complete UV-Vis spectrum, this was overcome by that the partially reduced W atoms served as recombination centers for photo-generated electrons and holes.

Nevertheless, in the case of the h-WO_3/TiO_2 NW sample, the addition of TiO_2 strongly influenced the photocatalytic activity, and resulted in a more effective photocatalyst compared to pure h-WO_3 or m-WO_3. It clearly shows the efficiency of ALD to reprogramme the surface properties of nanostructures by depositing nanolayers or nanoparticles on them, and thus to prepare photocatalysts with superior properties.

Mechanism of photocatalytic activities

It was revealed that m-WO_3 nanostructures typically overperform h-WO_3 nanostructures.[42] It is believed that structural differences play a key role in that. Photoluminescence studies (PL) confirmed that although h-WO_3 and m-WO_3 has similar emission pattern, h-WO_3 typically shows lower intensities in the luminescence spectrum.[42] This was previously attributed to the partially reduced state of h-WO_3 compared to m-WO_3 which arose from the presence of stabilizing cations in its hexagonal crystal structure. Between the reduced W atoms polaron transition could take place induced by the absorbed light.[78] Due to this, fewer light portion can actually play role in the excitation of electrons from the valence band to the conduction band of the h-WO_3 which explains the somewhat limited photocatalytic activities of h-WO_3 relative to m-WO_3.

One approach to mitigate e^-–h^+ pair recombination in single nanostructures is to form heterojunctions. In the event of beneficially aligned energy levels, the photo-generated charges can accumulate on different semiconductors which was found to produce longer-lived charges.[26] For a WO_3/TiO_2 system the electrons would favor to accumulate on the conduction band of WO_3 whereas holes would be preferably injected from the valence band of WO_3 to the valence band of TiO_2. This way the separation of the photo-generated charges can take place which supports photocatalytic surface reactions to take place. PL studies were also applied earlier to confirm the effective charge-separation in WO_3–TiO_2 systems.[67] It was found that the emission intensities for the nanocomposite *versus e.g.* TiO_2 was much lowered which was explained by the improved charge separation in the nanocomposite material.

Conclusions

In this paper h-WO_3 has been prepared by controlled annealing of $(NH_4)_xWO_3$ and by microwave hydrothermal synthesis to produce nanoparticles and nanowires, respectively. The two distinct morphologies were tested in photocatalytic application against m-WO_3 nanoparticles prepared also from $(NH_4)_xWO_3$. The h-WO_3 and m-WO_3 NPs were pure and consisted of 50–70 nm and 70–90 nm particles, respectively. The h-WO_3 NWs were single crystalline, 5–10 nm thick and several micrometer long. It was found that the h-WO_3 NWs had double as high photocatalytic activity compared to h-WO_3 NPs, and their performance was similar to m-WO_3 NPs.

Open Access Article. Published on 30 September 2016. Downloaded on 1/22/2026 5:10:50 PM.
This article is licensed under a Creative Commons Attribution 3.0 Unported Licence.

The h-WO_3 nanowires were then used as substrates for TiO_2 deposition by atomic layer deposition to study the nucleation characteristics of TiO_2 on hexagonal phase WO_3 for the first time. It was shown that the nucleation on the surface of h-WO_3 was substantially different from that of the m-WO_3. When TiO_2 was deposited by ALD onto h-WO_3 NWs, it did not form a continuous layer as on the surface of m-WO_3, but rather 5–10 nm particles. The unique nucleation pattern was understood by the lower surface OH density of h-WO_3 compared to m-WO_3 which did not serve dense enough nucleation sites for the ALD reactions to occur in a continuous manner. It was also presented that in contrast to yellow h-WO_3 NWs, the h-WO_3/TiO_2 NW turned to blue, due to the appearance of partially reduced W atoms. Our study is the first investigation of ALD nucleation on various WO_3 polymorphs and also the first example that different crystalline modifications of the same oxide material have so diverse effect on ALD growth.

When TiO_2 was grown on h-WO_3 NWs, it significantly increased the photocatalytic degradation rate, and resulted in a 65% increase in photocatalytic performance. Our results show that ALD is an outstanding tool to prepare composite photocatalysts.

Acknowledgements

D. Nagy acknowledges the Principal Career Development Scholarship awarded by the University of Edinburgh. I. M. Szilágyi acknowledges a János Bolyai Research Fellowship of the Hungarian Academy of Sciences and an OTKA-PD-109129 grant. Z. Baji, A. L. Tóth are acknowledged for contributing to the ALD depositions, ellipsometry and SEM-EDX measurements (Hungarian Academy of Sciences, Centre for Energy Research, Institute of Technical Physics and Materials Science, Budapest, Hungary).

References

1 H. Zhu and T. Lian, *Energy Environ. Sci.*, 2012, **5**, 9406–9418.
2 R. Das, S. B. A. Hamid, M. E. Ali, A. F. Ismail, M. S. M. Annuar and S. Ramakrishna, *Desalination*, 2014, **354**, 160–179.
3 H. Tong, S. X. Ouyang, Y. P. Bi, N. Umezawa, M. Oshikiri and J. H. Ye, *Adv. Mater.*, 2012, **24**, 229–251.
4 J. Byrne, P. Dunlop, J. Hamilton, P. Fernández-Ibáñez, I. Polo-López, P. Sharma and A. Vennard, *Molecules*, 2015, **20**, 5574.
5 N. Zhou, V. Lopez-Puente, Q. Wang, L. Polavarapu, I. Pastoriza-Santos and Q.-H. Xu, *RSC Adv.*, 2015, **5**, 29076–29097.
6 W. Wu, J. Changzhong and V. A. L. Roy, *Nanoscale*, 2015, **7**, 38–58.
7 W. Zhong, D. Li, S. Jin, W. Wang and X. Yang, *Appl. Surf. Sci.*, 2015, **356**, 1341–1348.
8 S. Yurdakal, V. Loddo, V. Augugliaro, H. Berber, G. Palmisano and L. Palmisano, *Catal. Today*, 2007, **129**, 9–15.
9 S. Malato, P. Fernández-Ibáñez, M. I. Maldonado, J. Blanco and W. Gernjak, *Catal. Today*, 2009, **147**, 1–59.
10 X. B. Chen, L. Liu, P. Y. Yu and S. S. Mao, *Science*, 2011, **331**, 746–750.
11 G. Halasi, I. Ugrai and F. Solymosi, *J. Catal.*, 2011, **281**, 309–317.
12 M. Gratzel, *Nature*, 2001, **414**, 338–344.
13 Q. Gu, J. L. Long, Y. G. Zhou, R. S. Yuan, H. X. Lin and X. X. Wang, *J. Catal.*, 2012, **289**, 88–99.
14 A. Fujishima, X. T. Zhang and D. A. Tryk, *Surf. Sci. Rep.*, 2008, **63**, 515–582.
15 O. Czakkel, E. Geissler, I. M. Szilágyi and L. Krisztina, 2013, **1**, 23–30.
16 S. Banerjee, D. D. Dionysiou and S. C. Pillai, *Appl. Catal., B*, 2015, **176–177**, 396–428.
17 Y. Zhang, Z. Jiang, J. Huang, L. Y. Lim, W. Li, J. Deng, D. Gong, Y. Tang, Y. Lai and Z. Chen, *RSC Adv.*, 2015, **5**, 79479–79510.
18 K. Teramura, T. Tanaka, M. Kani, T. Hosokawa and T. Funabiki, *J. Mol. Catal. A: Chem.*, 2004, **208**, 299–305.
19 T. Arai, M. Yanagida, Y. Konishi, Y. Iwasaki, H. Sugihara and K. Sayama, *Catal. Commun.*, 2008, **9**, 1254–1258.
20 Z.-G. Zhao and M. Miyauchi, *Angew. Chem., Int. Ed.*, 2008, **47**, 7051–7055.
21 D. S. Bohle and C. J. Spina, *J. Am. Chem. Soc.*, 2009, **131**, 4397–4404.
22 K. Tang, J. Zhang, W. Yan, Z. Li, Y. Wang, W. Yang, Z. Xie, T. Sun and H. Fuchs, *J. Am. Chem. Soc.*, 2008, **130**, 2676–2680.
23 G. Panthi, M. Park, H.-Y. Kim, S.-Y. Lee and S.-J. Park, *J. Ind. Eng. Chem.*, 2015, **21**, 26–35.
24 W. W. Zhong, Y. F. Lou, S. F. Jin, W. J. Wang and L. W. Guo, *Sci. Rep.*, 2016, **6**, 1–7.
25 Z.-F. Huang, J. Song, L. Pan, X. Zhang, L. Wang and J.-J. Zou, *Adv. Mater.*, 2015, **27**, 5309–5327.
26 Y. J. Wang, Q. S. Wang, X. Y. Zhan, F. M. Wang, M. Safdar and J. He, *Nanoscale*, 2013, **5**, 8326–8339.
27 R. Bogue, *Sens. Rev.*, 2014, **34**, 1–8.
28 D. L. Liao, C. A. Badour and B. Q. Liao, *J. Photochem. Photobiol., A*, 2008, **194**, 11–19.
29 H. Y. Wang, Y. Yang, X. Li, L. J. Li and C. Wang, *Chin. Chem. Lett.*, 2010, **21**, 1119–1123.
30 M. R. Gholipour, C.-T. Dinh, F. Beland and T.-O. Do, *Nanoscale*, 2015, **7**, 8187–8208.
31 D. Nagy, D. Nagy, I. M. Szilágyi and X. Fan, *RSC Adv.*, 2016, **6**, 33743–33754.
32 F. Amano, E. Ishinaga and A. Yamakata, *J. Phys. Chem. C*, 2013, **117**, 22584–22590.
33 Y. Xia, P. Yang, Y. Sun, Y. Wu, B. Mayers, B. Gates, Y. Yin, F. Kim and H. Yan, *Adv. Mater.*, 2003, **15**, 353–389.
34 T. Firkala, B. Fórizs, E. Drotár, A. Tompos, A. Tóth, K. Varga-Josepovits, K. László, M. Leskelä and I. M. Szilágyi, *Catal. Lett.*, 2014, **144**(5), 831–836.
35 F. Wang, X. Chen, X. Hu, K. S. Wong and J. C. Yu, *Sep. Purif. Technol.*, 2012, **91**, 67–72.
36 M. Shu-Quian, Z. De-Feng, Z. Xiao-Fei, Y. Guo-Cheng and L. Zhao-Hui, *J. Inorg. Mater.*, 2014, **29**, 605–613.
37 B. Lu, X. Li, T. Wang, E. Xie and Z. Xu, *J. Mater. Chem. A*, 2013, **1**, 3900–3906.
38 P. Guo, L. T. Meng and C. H. Wang, *Adv. Mater. Res.*, 2013, **850–851**, 78–81.

 This journal is © The Royal Society of Chemistry 2016

Open Access Article. Published on 30 September 2016. Downloaded on 1/22/2026 5:10:50 PM.
This article is licensed under a Creative Commons Attribution 3.0 Unported Licence.

39 E. Kamali Heidari, E. Marzbanrad, C. Zamani and B. Raissi, *Nanoscale Res. Lett.*, 2010, **5**, 370–373.
40 H. Long, W. Zeng and H. Zhang, *J. Mater. Sci.: Mater. Electron.*, 2015, **26**, 4698–4707.
41 I. M. Szilágyi, E. Santala, M. Heikkilä, M. Kemell, T. Nikitin, L. Khriachtchev, M. Räsänen, M. Ritala and M. Leskelä, *J. Therm. Anal. Calorim.*, 2011, **105**, 73–81.
42 I. M. Szilágyi, B. Fórizs, O. Rosseler, Á. Szegedi, P. Németh, P. Király, G. Tárkányi, B. Vajna, K. Varga-Josepovits, K. László, A. L. Tóth, P. Baranyai and M. Leskelä, *J. Catal.*, 2012, **294**, 119–127.
43 I. M. Szilágyi, J. Madarász, G. Pokol, P. Király, G. Tárkányi, S. Saukko, J. Mizsei, A. L. Tóth, A. Szabó and K. Varga-Josepovits, *Chem. Mater.*, 2008, **20**, 4116–4125.
44 A. Phuruangrat, D. J. Ham, S. J. Hong, S. Thongtem and J. S. Lee, *J. Mater. Chem.*, 2010, **20**, 1683–1690.
45 I. M. Szilágyi, E. Santala, M. Heikkilä, V. Pore, M. Kemell, T. Nikitin, G. Teucher, T. Firkala, L. Khriachtchev, M. Räsänen, M. Ritala and M. Leskelä, *Chem. Vap. Deposition*, 2013, **19**(4–6), 149–155.
46 V. Miikkulainen, M. Leskela, M. Ritala and R. L. Puurunen, *J. Appl. Phys.*, 2013, **113**, 021301.
47 M. N. Liu, X. L. Li, S. K. Karuturi, A. I. Y. Tok and H. J. Fan, *Nanoscale*, 2012, **4**, 1522–1528.
48 I. M. Szilágyi and D. Nagy, *J. Phys.: Conf. Ser.*, 2014, **559**, 012010.
49 H. Kim, H. B. R. Lee and W. J. Maeng, *Thin Solid Films*, 2009, **517**, 2563–2580.
50 I. M. Szilágyi, G. Teucher, E. Härkönen, E. Färm, T. Hatanpää, T. Nikiti, L. Khriachtchev, M. Räsänen, M. Ritala and M. Leskelä, *Nanotechnology*, 2013, **24**, 245701.
51 M. Knez, K. Nielsch and L. Niinistö, *Adv. Mater.*, 2007, **19**, 3425–3438.
52 S. Boyadjiev, V. Georgieva, L. Vergov, B. Zs, F. Gáber and I. M. Szilágyi, *J. Phys.: Conf. Ser.*, 2014, **559**, 012013.
53 I. M. Szilágyi, J. Pfeifer, C. Balázsi, A. L. Tóth, K. Varga-Josepovits, J. Madarász and G. Pokol, *J. Therm. Anal. Calorim.*, 2008, **94**, 499–505.
54 I. M. Szilágyi, S. Saukko, J. Mizsei, A. L. Tóth, J. Madarász and G. Pokol, *Solid State Sci.*, 2010, **12**, 1857–1860.
55 V. B. Patil, P. V. Adhyapak, S. S. Suryavanshi and I. S. Mulla, *J. Alloys Compd.*, 2014, **590**, 283–288.
56 T. Peng, D. Ke, J. Xiao, L. Wang, J. Hu and L. Zan, *J. Solid State Chem.*, 2012, **194**, 250–256.
57 J. Yu, L. Qi, B. Cheng and X. Zhao, *J. Hazard. Mater.*, 2008, **160**, 621–628.
58 D. Hunyadi, A. V. M. Ramos and I. M. Szilágyi, *J. Therm. Anal. Calorim.*, 2015, **120**, 209–215.
59 D. Hunyadi, I. Sajó and I. M. Szilágyi, *J. Therm. Anal. Calorim.*, 2014, **116**, 329–337.
60 A. Sonia, Y. Djaoued, B. Subramanian, R. Jacques, M. Eric, B. Ralf and B. Achour, *Mater. Chem. Phys.*, 2012, **136**, 80–89.
61 I. M. Szilágyi, S. Saukko, J. Mizsei, P. Király, G. Tárkányi, A. Tóth, A. Szabó, K. Varga-Josepovits, J. Madarász and G. Pokol, *Mater. Sci. Forum*, 2008, **589**, 161–165.
62 I. M. Szilágyi, L. Wang, P.-I. Gouma, C. Balázsi, J. Madarász and G. Pokol, *Mater. Res. Bull.*, 2009, **44**, 505–508.
63 C. Santato, M. Odziemkowski, M. Ulmann and J. Augustynski, *J. Am. Chem. Soc.*, 2001, **123**, 10639–10649.
64 A. Rey, P. García-Muñoz, M. D. Hernández-Alonso, E. Mena, S. García-Rodríguez and F. J. Beltrán, *Appl. Catal., B*, 2014, **154–155**, 274–284.
65 I. M. Szilágyi, I. Sajó, P. Király, G. Tárkányi, A. Tóth, A. Szabó, K. Varga-Josepovits, J. Madarász and G. Pokol, *J. Therm. Anal. Calorim.*, 2009, **98**, 707–716.
66 J. Zhang, W. Zhang, Z. Yang, Z. Yu, X. Zhang, T. C. Chang and A. Javey, *Sens. Actuators, B*, 2014, **202**, 708–713.
67 H. Shen, I.-R. Ie, C.-S. Yuan and C.-H. Hung, *Appl. Catal., B*, 2016, **195**, 90–103.
68 D. Nagy, T. Firkala, X. Fan and I. M. Szilágyi, *Eur. Chem. Bull.*, 2016, **5**, 40–42.
69 C. S. Hwang and A. Y. Yoo, *Atomic Layer Deposition for Semiconductors*, Springer, New York, Heidelberg, Dordrecht, London, 2014.
70 N. Pinna and M. Knez, *Atomic Layer Deposition of Nanostructured Materials*, Wiley-VCH Verlag & Co. KGaA, Weinheim, Germany, 2011.
71 M. Ritala and M. Leskelä, in *Handbook of Thin Films*, ed. H. S. Nalwa, Academic Press, Burlington, 2002, pp. 103–159, DOI: 10.1016/B978-012512908-4/50005-9.
72 S. Adhikari and D. Sarkar, *RSC Adv.*, 2014, **4**, 20145–20153.
73 J. Su, X. Feng, J. D. Sloppy, L. Guo and C. A. Grimes, *Nano Lett.*, 2010, **11**, 203–208.
74 G. Liu, L.-C. Yin, J. Wang, P. Niu, C. Zhen, Y. Xie and H.-M. Cheng, *Energy Environ. Sci.*, 2012, **5**, 9603–9610.
75 H. Dong, Z. Wu, F. Lu, Y. Gao, A. El-Shafei, B. Jiao, S. Ning and X. Hou, *Nano Energy*, 2014, **10**, 181–191.
76 J. K. Yang, X. T. Zhang, H. Liu, C. H. Wang, S. P. Liu, P. P. Sun, L. L. Wang and Y. C. Liu, *Catal. Today*, 2013, **201**, 195–202.
77 L. Yang, Z. Si, D. Weng and Y. Yao, *Appl. Surf. Sci.*, 2014, **313**, 470–478.
78 S. H. Lee, H. M. Cheong, C. E. Tracy, A. Mascarenhas, D. K. Benson and S. K. Deb, *Electrochim. Acta*, 1999, **44**, 3111–3115.